3.3. Insulating Cylindrical Inclusion (ICI) Experiments

As previously discussed, computational validation exercises were performed to assess the capability of the computer code FEMEIT to produce accurate reconstructions of a spatially varying conductivity field. FEMEIT has also been validated by comparison to experiments employing known and well controlled conductivity fields.

A nontrivial spatially varying conductivity field was produced by inserting an insulating cylindrical inclusion (ICI) into a homogeneous conducting liquid, as shown in Figure 33. More specifically, insulating tubes of known diameters were placed within the EIT probe ring employing strip electrodes, and the EIT system was used to measure the electrode voltages during current flow. These electrode voltages were then used as inputs to the code FEMEIT to determine the diameter and position of the ICI. A limited number of experiments were also performed using the EIT probe ring with point electrodes. These data sets were analyzed using the code EITA3D, as appropriate for point, rather than strip, electrodes.

3.3.1. ICI Experimental Setup

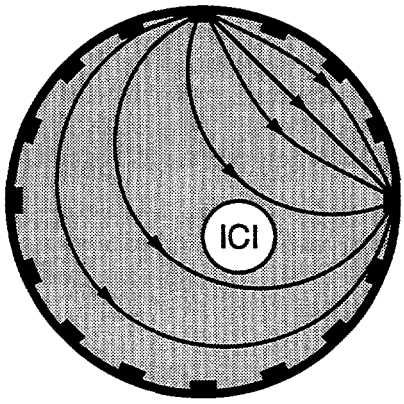

Figure 33. Schematic diagram of EIT with an insulating cylindrical inclusion (ICI).

The EIT probe ring employing 16 strip electrodes was used for the FEMEIT validation experiments. To create a two-dimensional field, the probe ring was capped off on the bottom with a lucite plate mounted flush to the bottom of the electrodes, a PVC cylinder of known diameter (the ICI) was placed eccentrically at a particular position within the probe ring, and the probe ring was filled with water to the top of the electrodes.

The EIT probe ring employing 16 point electrodes was used for the EITA3D validation experiments. The probe ring, 2 diameters in height, was capped at the bottom, a lucite cylinder of known diameter (the ICI) was placed concentrically within the probe ring, and the probe ring was filled with water to the top.

The same electronics hardware was used for both probe rings. A small amount of salt was added to the water as needed to bring the liquid conductivity to roughly 1 mS/cm. The internal capacitance and resistance of the electronics were adjusted to yield minimal signal-to-noise ratio for these conditions.

3.3.2. ICI Experimental Results from EIT

For the FEMEIT validation experiments, a 6.92 cm (2.725 inch) hollow PVC tube was used as the ICI. Two different positions of the ICI were examined, one eccentric and one concentric with respect to the probe ring. For each position, all EIT voltages were measured 6400 times each, which required roughly 10 minutes. The averages of these measurements were the inputs to FEMEIT. To reconstruct the size and position of the ICI, FEMEIT used a conductivity function of the form:

$$\sigma = C_1\left\{1+\frac{P_1}{2}\left[\tanh\left(\frac{r-C_2}{P_2}\right)-\tanh\left(\frac{r+C_2}{P_2}\right)\right]\right\}, \tag{55}$$

where $r^2 = (x-C_3)^2+(y-C_4)^2$, $\{C_1, C_2, C_3, C_4\}$ are adjustable conductivity parameters, and $\{P_1, P_2\}$ are nonadjustable parameters. This function represents a circular region of radius C_2 centered at (C_3, C_4) with a boundary thickness proportional to $2P_2$, well inside of which the conductivity is approximately $C_1(1-P_1)$ and well outside of which the conductivity is approximately C_1. If P_1 is chosen close to but smaller than unity and P_2 is taken to be small compared with C_2, this function represents an insulating cylinder, where its position, radius, and external conductivity are free to vary. FEMEIT calculations were performed using mesh E (the most highly refined mesh from the numerical validation exercises, see Figure 24) and the above function with the nonadjustable parameters assigned values of $1-P_1 = 0.02$ and $2P_2 = 0.1$, where the lucite cylinder has been normalized to unity radius. The sizes and positions of the ICI reconstructions are shown in Figure 34 and agree well with the experimental sizes and positions, also shown in Figure 34. No dependence on the initial values of the adjustable parameters was seen in the reconstructions: the calculations consistently yield values of 6.91 cm (2.72 inch) for the ICI diameter.

For the EITA3D validation experiments, long hollow lucite tubes were used as the ICIs. Two different concentrically-positioned ICIs and two cases without ICIs were examined, as shown in Table 2. For each ICI, all EIT voltages were measured 6400 times each, and the averages of these measurements were the inputs to EITA3D. To reconstruct the size of the ICI, EITA3D used a conductivity function (based on FIDAP voltages) of the form:

$$\sigma = \sigma_1/C_1,\ \sigma_1 = \begin{cases} 0\ , & 0 \le r/R < C_2 \\ 1\ , & C_2 \le r/R \le 1 \end{cases} \text{ with } 0 \le C_2 < 1\,. \tag{56}$$

The agreement between the experimental and computational sizes is fairly good although EITA3D consistently overpredicts the ICI diameter (in fact, small-diameter objects can be predicted when none are present, as shown in Table 2). The cause of this overprediction is not known at present.

Table 2. EITA3D reconstructions of ICI diameters.

Experimental diameter	Reconstructed diameter
0 cm (0 inch)	1.04 cm (0.41 inch)
0 cm (0 inch)	1.55 cm (0.61 inch)
5.72 cm (2.25 inch)	5.99 cm (2.36 inch)
10.19 cm (4.01 inch)	10.52 cm (4.14 inch)

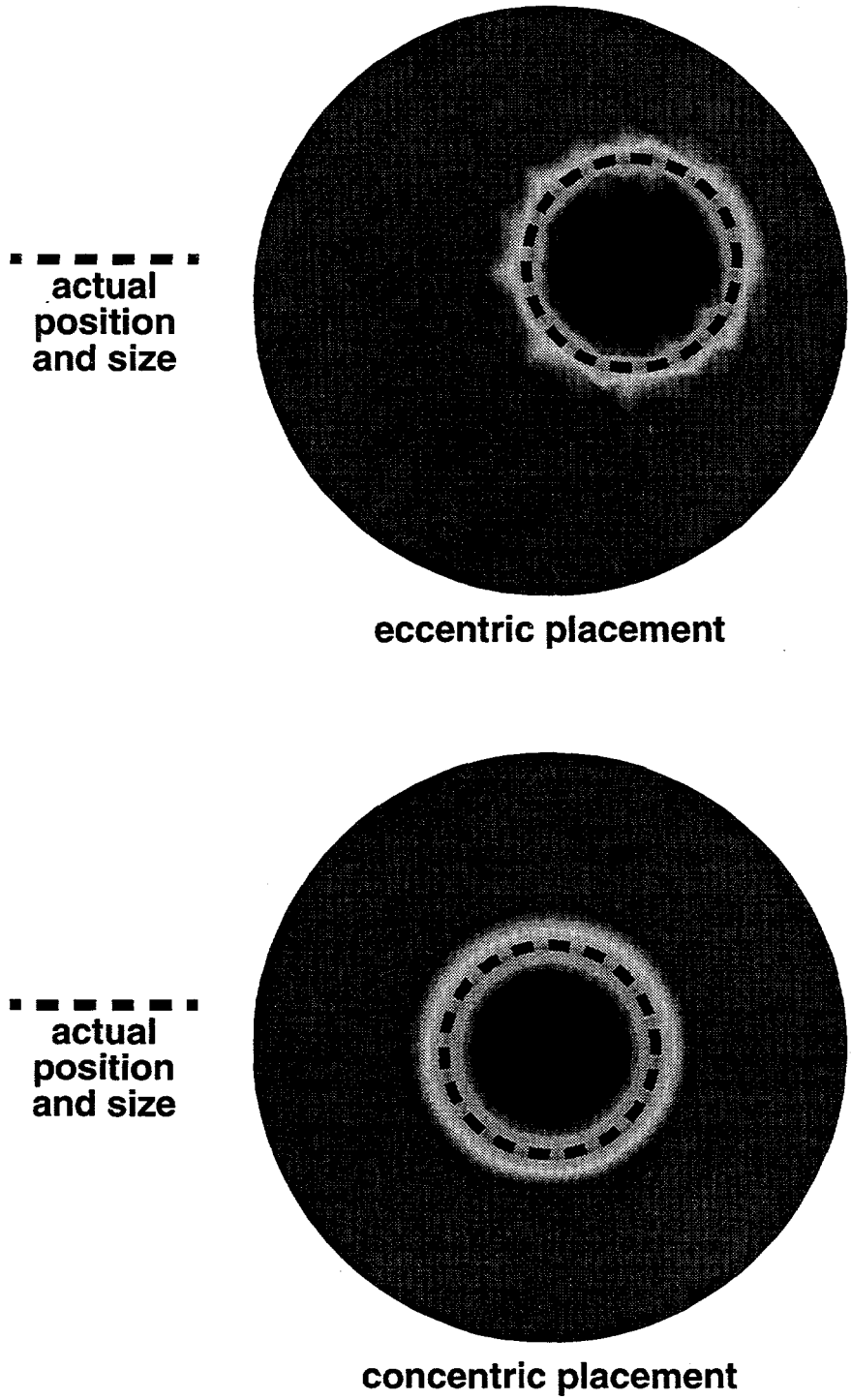

Figure 34. EIT reconstructions of insulating cylinders using strip electrodes.

4. Experimental Testbeds and Results

4.1. Transparent Bubble Column (TBC) Experiment

A transparent bubble column (TBC) experiment was used as a test bed for diagnostics development and is shown in Figure 35. Although not capable of operation at the high pressures and temperatures of industrial interest, this bubble column facilitated simultaneous implementation and rapid modification of multiple types of diagnostic techniques. Optical techniques, such as flow visualization and LR, can be applied because of the transparent nature of the TBC experiment. Pressure-based techniques, such as DP, can be used if pressure taps penetrate the side wall. Radiation-based techniques, such as GDT, are facilitated by virtue of the side wall, which was fairly thin and made of low-density material because of the absence of imposed pressurization or heating. Electrical techniques, such as BEI, EIT, and the EBP, can be applied without concern about the effects of current-transport through the side wall since it is insulating. Geometric modifications, such as installation of alternate spargers or probe rings, could also be carried out easily and quickly.

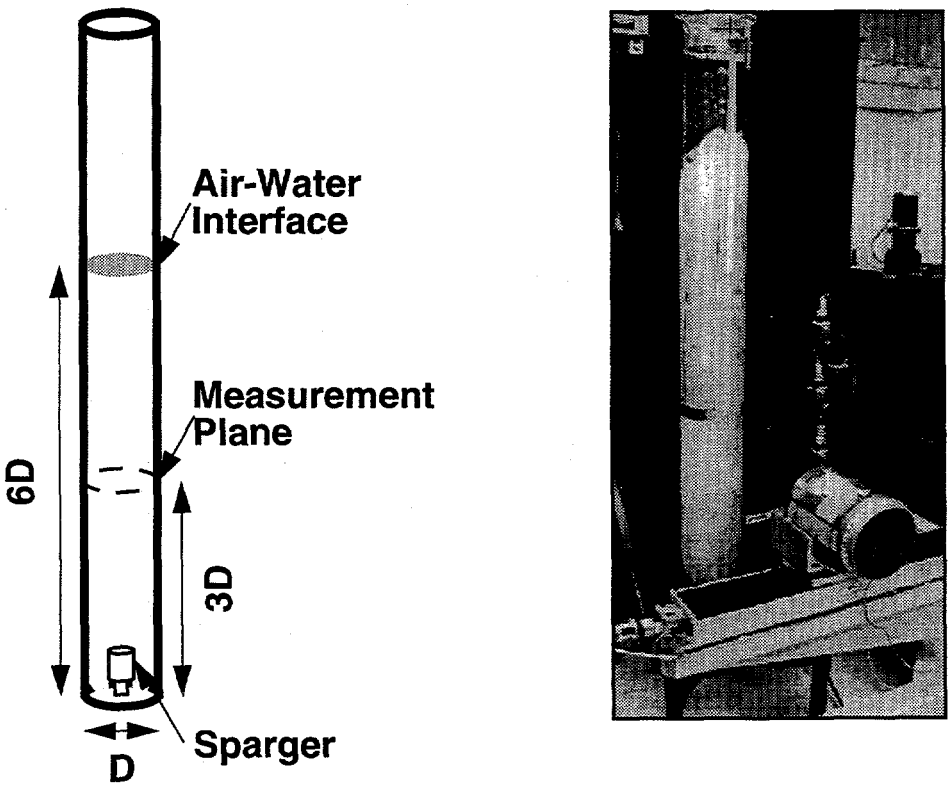

Figure 35. The transparent bubble-column (TBC) experiment.

4.1.1. TBC Experimental Setup

The TBC experiment is a lucite tube held in place by a unistrut frame (see Figure 35). The lucite tube has outer and inner diameters of 20.32 cm (8 inch) and 19.05 cm (7.5 inch), respectively, a wall thickness of 0.635 cm (0.25 inch), and a height of 1.83 m (72 inch). The working fluids generally are air and water although some other liquids can be used, and operation is at ambient temperature and pressure. To preclude overflow during air flow, the column is filled with water to an initial height of only 1.14 m (45 inch), a height-to-diameter ratio of 6. Gas is introduced near the bottom of the column via a sparger. Two spargers have been employed to date. The original sparger used in the TBC experiment was a 9 cm diameter ring spiral made from 0.635 cm (0.25 inch) OD copper tubing in which 12 downward-facing holes of 0.08 inch diameter were drilled at equal azimuthal intervals. Another sparger was subsequently developed and installed in the TBC experiment, as shown in Figure 36. This sparger is a hollow toroidal ring with a 10.16 cm (4 inch) center-line diameter and is made from stainless steel tubing with a 0.95 cm (0.375 inch) diameter and a 0.165 cm (0.065 inch) wall through which 10 downward-facing holes of 0.159 cm (0.0625 inch) diameter have been drilled at equal azimuthal separations. As currently configured, air flow rates of up to 600 lpm (liters per minute) are routinely achievable, which correspond to gas superficial velocities up to 35 cm/s. It is also possible to introduce a significant amount of a third phase of solid particulates into the column, such as sand or glass spheres.

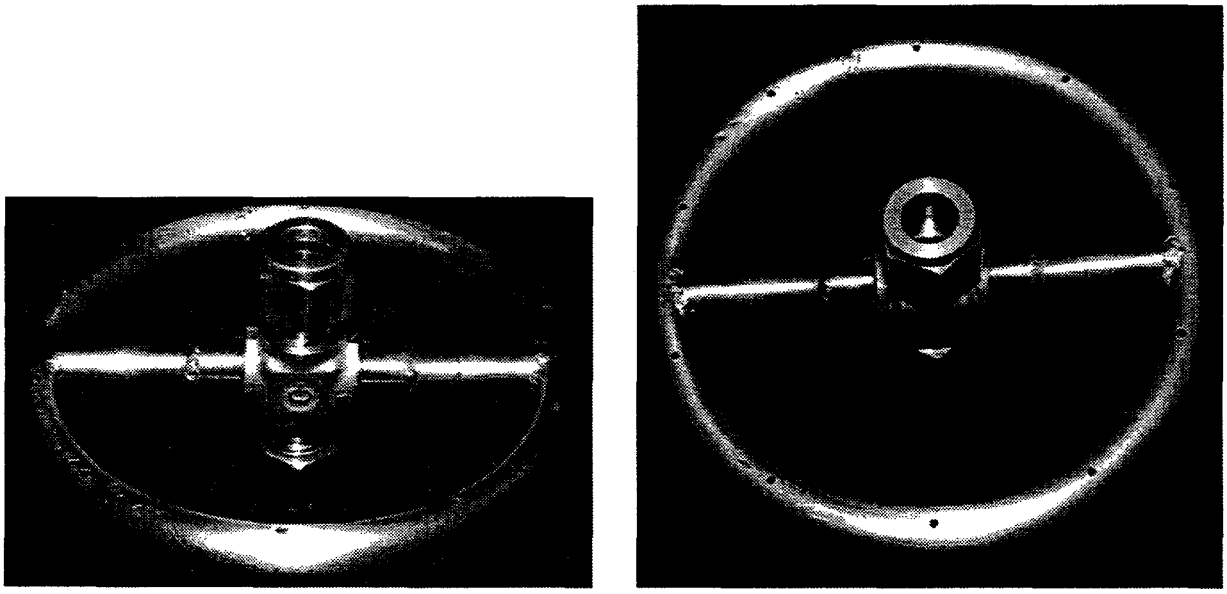

Figure 36. Sparger (final design) in TBC.

The LR and DP diagnostics are applied routinely to the TBC experiment. For the LR technique, the gas-liquid interface can be observed visually and compared with ruled markings on the column for quantitative values. If necessary, a video camera and a VCR can be used to record this information for post-test analysis or image-processing. For the DP technique, five pressure transducers have been installed to measure the pressure within the column. These transducers are located at vertical intervals equal to the inner diameter and resolve axial (and temporal) variations in the pressure.

Additional diagnostics can be installed as needed for development, validation, and data collection. GDT can be applied directly with no modification to the TBC experiment simply by positioning the traverse appropriately so that the arms surround the lucite column. Applying BEI or EIT requires installation of the corresponding probe ring within the column. This was facilitated by sectioning the column into two halves and fabricating short connecting sections that seal to the column and probe-ring exteriors using O-rings. The EBP was deployed by installing a special lucite section into the column, which contains a tap through which the EBP support is inserted.

Applying electrical techniques imposed two additional constraints on the TBC experiment. First, the presence of a grounded conductor anywhere in the liquid-filled portion of the column was found to exert a strong effect on electrical data. To prevent this from occurring, all conducting fittings were removed or electrically isolated, including the sparger. Second, it was discovered that the evaporation produced by dry air flowing through the water can cool it by as much as 2-4 K over an hour of operation. Since the electrical conductivity of water is temperature-dependent and decreases with decreasing temperature, the cooler water appears more insulating to electrical techniques. If this effect is ignored, the cooled water causes electrical techniques to register the presence of air even when no air was present, as shown in Figure 37. To compensate for evaporative cooling, three controllable 80-W immersion heaters were installed in the column and are used to maintain the water temperature at a prescribed value to 0.1 K.

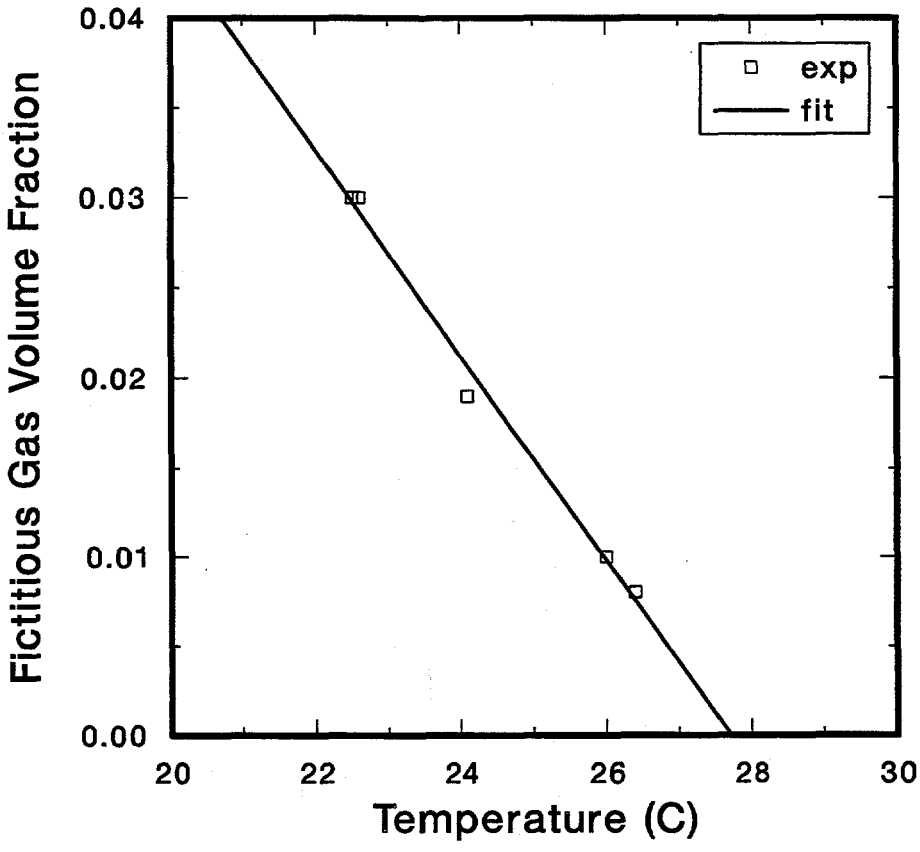

Figure 37. Temperature-dependent electrical conductivity can give spurious results.

4.1.2. TBC Experimental Results

Gas-liquid two-phase flow experiments and gas-liquid-solid three-phase flow experiments have been performed in the TBC experiment (Torczynski et al., 1996a). Air and water were the working fluids, and sand (silicon dioxide particles with diameters in the 0.1-0.4 mm range) was used for the solid particulate phase in the three-phase experiments. The original spiral-ring sparger was used for these experiments, and the column was filled with the prescribed amount of sand (none for the two-phase experiments) and with sufficient water so that the interface was 6 diameters above the bottom of the column in the absence of air flow.

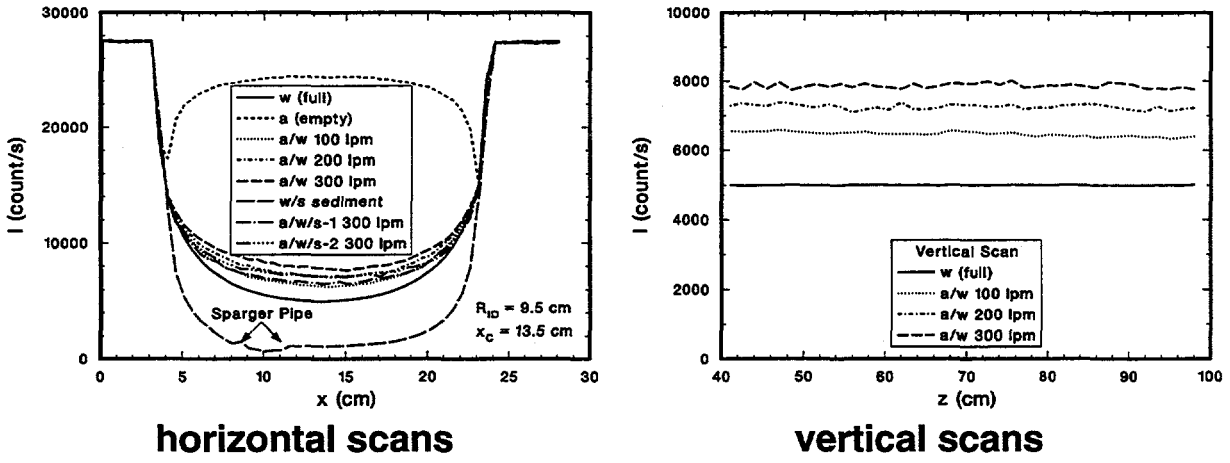

Figure 38. Count-rate results from GDT in TBC.

GDT scans were performed at various locations for several flow conditions in the TBC experiment. Count-rate results for all of these scans are shown in Figure 38, in which "a", "w", and "s" denote air, water, and sand, respectively. Horizontal GDT scans with the column centered at x = 13.5 cm were performed at two vertical locations: 3 diameters above the bottom of the column for all flow conditions and in the sediment layer that exists near the bottom of the column prior to initiating air flow for three-phase experiments. For all horizontal scans, attenuation measurements were made at 0.5 cm intervals across the width of the column. This yielded 38 horizontal positions, which previously were shown to be sufficient to produce an accurate reconstruction of the material distribution for axisymmetric conditions. Horizontal GDT scans were performed with the column empty of water (full of air) and full of water (empty of air) for calibration purposes, with gas-liquid flow at air flow rates of 100, 200, and 300 lpm, and with gas-liquid-solid flow at an air flow rate of 300 lpm, where an air flow rate of 300 lpm corresponds to a gas superficial velocity of 17.7 cm/s. Vertical GDT scans were also performed for the gas-liquid flow conditions above, where attenuation measurements were made directly through the diameter at 1.5 cm intervals in the vertical direction from 40 cm to 100 cm above the bottom of the column. The purpose of the vertical scans was to verify that the material distribution did not change significantly in the vertical direction, which is indeed seen to be the case from Figure 38.

For comparison purposes, two other methods were used to yield information about the gas volume fraction. First, LR measurements were performed to determine the average gas volume fraction for the entire column. Second, DP measurements were performed to determine the average gas volume fraction in a one-diameter length of the column centered about the GDT measurement plane.

Figure 39 shows the GDT results for the gas-liquid and gas-liquid-solid flows described above in the TBC experiment. Four of the plots (a-d) in Figure 39 show the variation of the normalized mixture attenuation as a function of horizontal or radial position for the flow conditions that were examined. The symbols indicate the experimentally measured normalized attenuation coefficient averaged along the paths (rays), essentially the values $\{(x_i, \psi_i)\}$ required by the GDT reconstruction algorithm. The dashed curves are polynomial fits to these values using quartic polynomials of the form $b_0 + b_1(x/R)^2 + b_2(x/R)^4$. Quartic polynomials were chosen because polynomials of lower degree produced much less satisfactory fits and polynomials of higher degree did not produce significantly better fits. The dotted curves are the resulting polynomial reconstructions of the radial variation of the attenuation coefficient and as such have the form $a_0 + a_1(r/R)^2 + a_2(r/R)^4$.

For two-phase flow, knowledge of the normalized mixture attenuation coefficient is sufficient to permit determination of the phase volume fractions of the two phases. The gas-volume-fraction radial profiles for the two-phase conditions are shown in the fifth plot (e) for the air flow rates examined. As is typical of gas-liquid flows in bubble columns, the gas volume fraction is largest on axis, monotonically decreases toward the side wall, and increases with increasing gas flow rate. For this particular experiment, the gas-volume-fraction radial profiles are also observed to become more blunt with increasing gas flow rate. This observation is probably not true in general, however. Table 3 shows a comparison between the average gas volume fractions determined from the LR, DP, and GDT techniques. The agreement is reasonably good, particularly since each technique averages over a different volume of the column (the entire column for LR, a cylinder that is one diameter high for DP, and a thin cross-sectional slice for GDT). Also, the GDT measurements indicate a modest but systematic departure from axisymmetry, so it is not altogether surprising that gas-volume-fraction values determined by applying an axisymmetric GDT reconstruction algorithm should depart slightly but systematically from values determined by other techniques not assuming axisymmetry. Unfortunately, it is not possible to determine the precise amount of departure from axisymmetry without multiple projections (i.e. scans from different azimuthal angles). It was this observed asymmetry that motivated the improved sparger design, previously discussed.

Table 3. Average gas volume fractions in TBC.

Air Flow (lpm)	Solid Phase	Sup. Vel. (cm/s)	LR	DP	GDT
100	absent	5.9	0.11	0.11	0.12
200	absent	11.8	0.17	0.17	0.19
300	absent	17.7	0.22	0.20	0.24
300	present	17.7	-	-	0.23

For three-phase flow, GDT and the phase rule (phase volume fractions sum to unity) do not provide enough information to determine all three unknown phase-volume-fraction spatial distributions (i.e. for air, water, and sand). To achieve closure, an additional relation is required. One possible assumption is that all of the sand suspended in the flow (as differentiated from the sediment layer of sand at the bottom of the column) is distributed uniformly within the liquid phase: the solid and liquid volume fractions are proportional throughout the flow. Since the bubble-induced mixing appears strong, this assumption seems reasonable. Note, however, that this assumption constrains the radial variations of the liquid and solid volume fractions to be proportional.

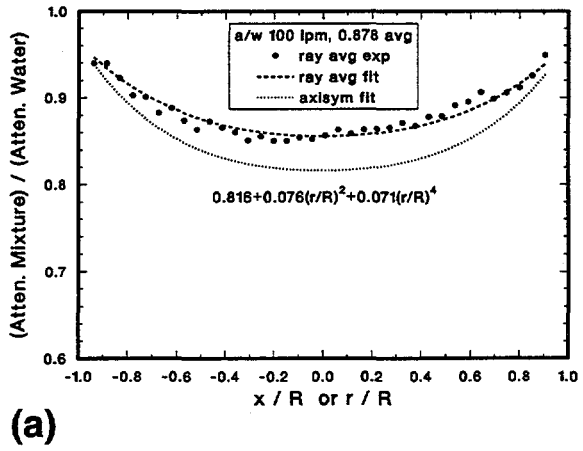

(a)

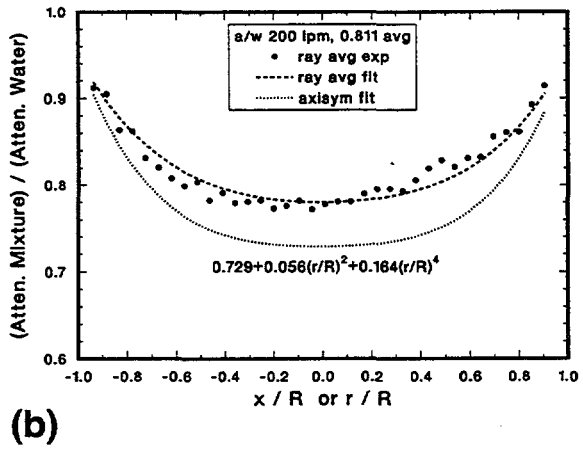

(b)

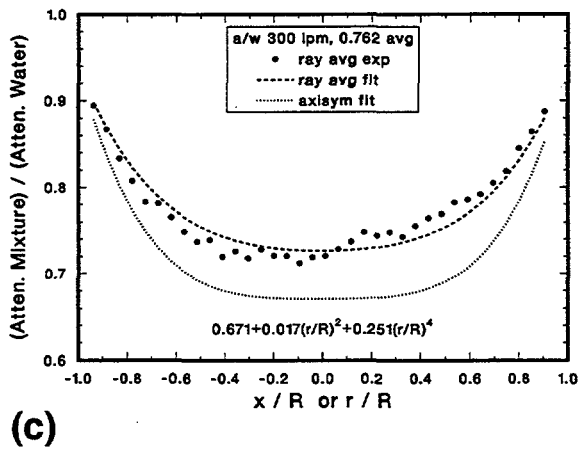

(c)

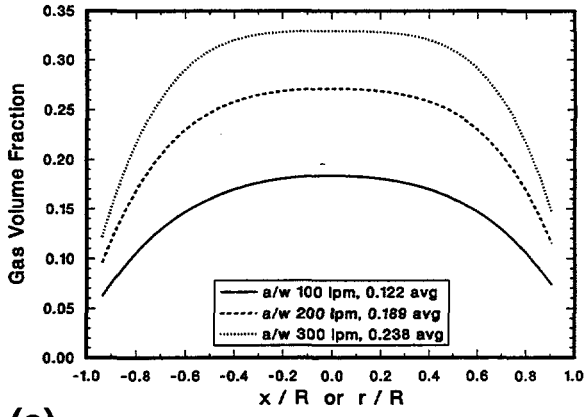

(e)

Mixture attenuation coefficients:
- (a) 100 lpm, gas-liquid
- (b) 200 lpm, gas-liquid
- (c) 300 lpm, gas-liquid
- (d) 300 lpm, gas-liquid-solid

Experimental results for attenuation:
- Symbols: averages along path (ray)

Computational results for attenuation:
- Dashed curves: polynomial fits to symbols
- Dotted curves: polynomial reconstructions

Gas-volume-fraction summary plot:
- (e) 100, 200, 300 lpm, gas-liquid

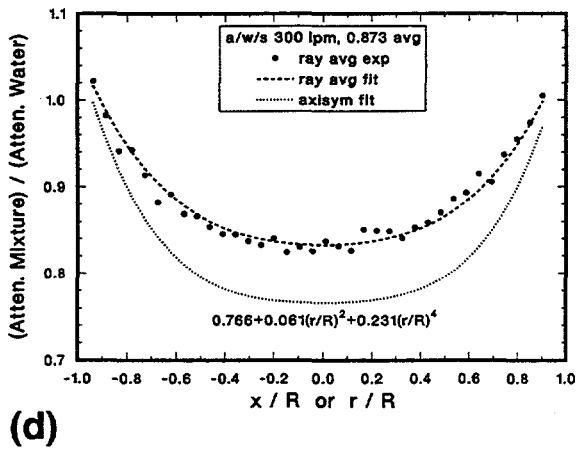

(d)

Figure 39. Gas-liquid and gas-liquid-solid results from GDT in TBC.

To determine the constant of proportionality, it is necessary to determine the amount of sand suspended during air flow. This was accomplished by measuring the height of the sediment layer that remained unsuspended during air flow and using the known volume fraction of sand in the sediment layer, 0.63. This quantity had been determined prior to the experiments in the following manner. A large graduated cylinder was filled with 1000 cm^3 of water (991 g mass) and 1000 cm^3 of (initially dry) sand (1534 g mass). The water-sand mixture was composed of two regions, a sediment region on the bottom and a water region on the top. The total volume of these two regions was measured to be 1630 cm^3, yielding a sand volume of 630 cm^3. Thus, densely packed sand has a volume fraction of 0.63. As a check, the intrinsic mass density of the sand grains was calculated from the above mass and volume and found to be 2.44 g/cm^3, which is close to the value of 2.65 g/cm^3 for pure SiO_2 (cf. Weast, 1973). An additional check comes from the GDT horizontal scan of the sediment without air flow, which indicated a normalized attenuation coefficient of 1.937 for the sand-water sediment. Since the sediment has a sand volume fraction of 0.63 and a water volume fraction of 0.37, the normalized attenuation coefficient for sand is 2.487. Since the attenuation coefficient of water is 0.0858 cm^{-1}, the experimentally determined attenuation coefficient for sand is 0.2134 cm^{-1}, which is close to the theoretical value of 0.2041 cm^{-1} for pure SiO_2 (Lamarsh, 1983).

Prior to initiating air flow, 8.37 kg of sand, with an equivalent height of 19.1 cm, was added to the TBC experiment, which had previously been filled with water to a height of 76.2 cm. When an air flow of 300 lpm was initiated, the undisturbed sediment layer remaining on the bottom was found to be 7.6 cm thick, so the suspended water and sand (i.e. not in the sediment region) have effective heights of 73.4 cm and 7.2 cm, respectively. The ratio of these heights yields a value of 0.098 for the constant of proportionality relating the sand and water volume fractions (valid only for this particular experiment). Figure 39 shows the normalized mixture attenuation as a function of horizontal or radial position for these flow conditions. Note that the normalized mixture attenuation exceeds unity near the side wall. This is possible because the attenuation coefficient of sand is more than twice the attenuation coefficient of water, which was used in the normalization. Figure 40 shows the volume-fraction radial profiles for gas-liquid and gas-liquid-solid flow at 300 lpm, with average values shown in the plot legends. Interestingly, the solid phase had only a minimal effect on the air volume fraction, both in average value and in radial variation. This observation should not be assumed to apply in general to other experimental conditions.

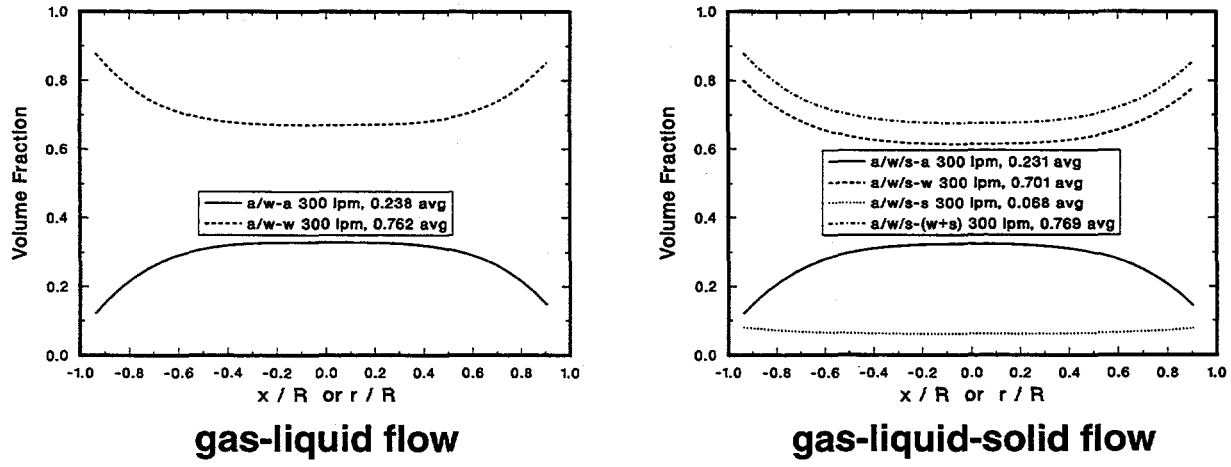

Figure 40. Phase volume fraction results from GDT in TBC.